Phys. Status Solidi B, 1–7 (2016) / **DOI** 10.1002/pssb.201600260

physica status solidi b
www.pss-b.com
basic solid state physics

Transport through graphene nanoribbons: Suppression of transverse quantization by symmetry breaking

Florian Libisch*, **Andrej Kliman, Stefan Rotter, and Joachim Burgdörfer**

Institute for Theoretical Physics, Vienna University of Technology, Wiedner Hauptstraße 8-10/136, A-1040 Vienna, Austria

Received 25 April 2016, revised 11 July 2016, accepted 14 July 2016
Published online 6 August 2016

Keywords disorder, graphene, quantization, transport

* Corresponding author: e-mail florian.libisch@tuwien.ac.at, Phone: +43-1-58801-13608, Fax: +43-1-58801-13699

We investigate transport through graphene nanoribbons in the presence of disorder scattering. We show that size quantization patterns are only present when SU(2) pseudospin symmetry is preserved. Symmetry breaking disorder strongly suppresses signatures of transverse quantization due to the inherent entanglement of pseudospin and transverse quantum numbers in graphene. To quantitatively distinguish the influence of symmetry breaking and symmetry conserving disorder on transport, we consider weak localization: we observe a transition from weak antilocalization to weak localization as symmetry-breaking disorder is introduced. We discuss implications for experimental observations of size quantization signatures.

1 Introduction Graphene, the first two-dimensional solid [1], features remarkable electrical and mechanical properties that open up possibilities for many new and intriguing applications [2]. While properties of the perfect honeycomb lattice and its consequences for electronic structure and dynamics are well understood, the effect of disorder caused by local distortions of the graphene lattice, graphene–substrate interaction, or charged impurities on the unique properties of graphene remains the focus of theoretical investigations [3–9]. On general grounds, local symmetry breaking in low-dimensional systems is expected to have more pronounced effects than in 3D bulk materials. Investigations of scattering at long-range potentials [10] demonstrate the importance of the underlying symmetry for conductance properties. Investigations of the local density of states near edges [11, 12] or at bulk vacancies [13–17] show a pronounced structure associated with the formation of quasilocalized states that strongly influence the material properties. In this article, we demonstrate that not only the spatial extension of defects (i.e., short range vs. long range), but also their symmetry breaking property is crucial: we find a remarkably strong sensitivity of quantum transport and of weak localization in graphene nanoribbons to very low concentrations of single vacancies that break the SU(2) pseudospin symmetry associated with the triangular sublattices of graphene. By contrast, point defects that conserve this symmetry have a substantially weaker effect. We simulate transport through disordered nanoribbons of realistic size described by a tight-binding Hamiltonian. To interpret our numerical results, we consider two simpler models: a continuous Dirac-like equation and a quasi-classical Monte-Carlo simulation. We identify pseudospin non-conserving scattering at lattice vacancies to be the key for the breakdown of size quantization.

2 Model Graphene can be described in tight-binding approximation by the Hamiltonian [18]

$$H = \sum_{i,s} |\phi_{i,s}\rangle\, V_i\, \langle\phi_{i,s}| - \sum_{(i,j),s} \gamma_{i,j}\, |\phi_{i,s}\rangle\, \langle\phi_{j,s}| + \text{h.c.}, \tag{1}$$

where the sum (i, j) extends over pairs of lattice sites, $|\phi_{j,s}\rangle$ is the tight-binding orbital with spin s at lattice site j, V_i is a locally varying potential, and $\gamma_{i,j}$ is the hopping matrix element between lattice sites i and j. For improved accuracy, we describe the hexagonal graphene lattice using third-nearest-neighbor coupling (for details see Ref. [12]). We consider

ensembles of ribbons with an average width of up to 60 nm corresponding to ≈ 300 unit cells in transverse direction (y) orthogonal to the direction of transport (x) using the modular recursive Green's function method (MRGM) [12, 20]. A magnetic field is included by a Peierls phase factor. We perform ensemble averages over, typically, 100 different disorder realizations to eliminate any non-generic feature.

We analyze the implications of the numerical results with the help of simpler models. One of them employs the Dirac-like bandstructure of graphene. Close to the Fermi energy, the band structure of Eq. (1) can be approximated (assuming that $V_i \ll \gamma_{i,j}$) by a conical dispersion relation around the K point [21],

$$E(k + k_K) = E(k_K) + k\partial_k E(k_K) + \mathcal{O}(k_K^2) \approx v_F|k|, \tag{2}$$

with the Dirac-like Hamiltonian,

$$H = \hbar v_F \begin{pmatrix} 0 & \partial_x + i\partial_y \\ \partial_x - i\partial_y & 0 \end{pmatrix} + \mathbb{1} \cdot V(\mathbf{x}), \tag{3}$$

where we have set $E(k_K) = 0$. Equation (3) ignores both the length scale of the graphene lattice constant $a = 1.4$ Å and the broken rotational symmetry of the cone due to the hexagonal lattice structure, an effect known as trigonal warping [2]. Eigenfunctions of Eq. (3) on an infinitely extended sheet ($V = 0$) are plane waves $|k\rangle$ where the direction of motion θ_k,

$$\theta_k = \tan^{-1}(k_y/k_x), \tag{4}$$

is coupled to the AB-sublattice degree of freedom [2],

$$|\mathbf{k}\rangle = e^{i\mathbf{k}\cdot\mathbf{r}} \left(|A\rangle + e^{i\theta_k}|B\rangle\right)/\sqrt{2}. \tag{5}$$

The Hamiltonian H preserves the SU(2) pseudospin projection (or helicity) $h = (\boldsymbol{\sigma} \cdot \mathbf{k})/|\mathbf{k}|$ along $\hat{k}$, i.e., the angle θ_k ($\boldsymbol{\sigma}$ is the vector of the Pauli matrices). Conservation of pseudospin is a direct consequence of the symmetry between the two sublattices A and B. Furthermore, the band structure features *two* non-equivalent cones ("valleys") at the K and K' points in the reciprocal lattice. This additional degeneracy allows to represent the low-energy band-structure near $E = 0$ in terms of Dirac-like four-spinors $|\psi\rangle = (\psi_A^K, \psi_B^K, \psi_A^{K'}, \psi_B^{K'})$ with amplitudes for the AB-sublattice in real space and for the KK' points in reciprocal space. The sign of θ_k is reversed upon transition from K to K'. Note that physical spin s is not included in the present analysis.

3 Lattice defects One of the consequences of pseudospin conservation is the suppression of backscattering [2]. If the scattering potential commutes with the helicity operator, the first-order transition probability P for scattering

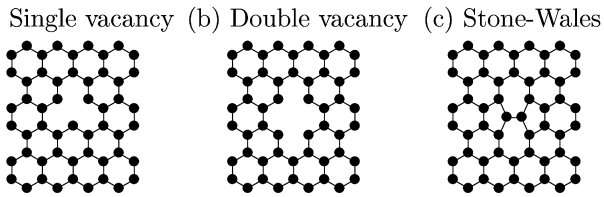

Figure 1 Defects in graphene nanoribbons: (a) single vacancy, breaking the degeneracy between the two sublattices; (b) double vacancy which equally affects both sublattices; (c) Stone–Wales deformation: four hexagons are replaced by pairs of pentagons and heptagons.

$|\mathbf{k}\rangle \to |\mathbf{k}'\rangle$ is proportional to

$$P(\mathbf{k} \to \mathbf{k}') = \left|\left\langle \mathbf{k}' \right| V \left|\mathbf{k}\right\rangle\right|^2 \propto \cos^2[(\theta_\mathbf{k} - \theta'_{\mathbf{k}'})/2], \tag{6}$$

which vanishes for $\left|\theta_\mathbf{k} - \theta'_{\mathbf{k}'}\right| = \pi$, i.e., for backscattering. If, however, the lattice structure is locally disturbed, e.g., by a single vacancy, such that the sublattice symmetry is broken and pseudospin is no longer conserved, Eq. (6) no longer applies and backscattering becomes possible. Indeed, for single vacancies, simple algebra proves the emergence of states localized at only one sublattice [9], in contrast to the plane wave solutions of Eq. (5). However, if the same number of atoms are removed from both lattices (i.e., by forming a double vacancy, Fig. 1b), no such localized states are observed [9]. More generally, differential cross-sections for scattering at local defects that preserve the SU(2) pseudospin symmetry should obey Eq. (6) while defects that locally break it allow for scattering in arbitrary direction, in particular for isotropic s-wave scattering in the long-wavelength limit ($k \to 0$),

$$P(\mathbf{k} \to \mathbf{k}') \propto \text{const.} \tag{7}$$

We consider three different lattice defects (Fig. 1), which locally perturb the electronic structure and, thus, introduce disorder. The simplest defect is a point defect residing on a single carbon atom. Such a defect can be caused, e.g., by chemical absorption of molecules [22], such as hydrogen, forming a covalent bond with the p_z orbital of a carbon atom, locally changing the electronic configuration from sp^2 to sp^3. Consequently, the p_z orbital of this carbon atom no longer contributes to the electronic bandstructure of graphene. In a tight-binding approximation, this can be modeled by a single (electronic) lattice vacancy, i.e., one carbon atom is effectively removed from the graphene lattice (see Fig. 1a). This defect features a localized state [13–15, 23] Since the number of active sites on both sublattices becomes different, states localized on one sublattice emerge [9]. We consider an ensemble average over many configurations of randomly placed point defects with a relative defect density as small as $n_i = 10^{-5}$ impurities per carbon. As a second class of defects, we consider double vacancies as recently investigated [24], i.e., we remove both atoms of a unit cell (see Fig. 1b). Double vacancies are pseudospin conserving as both the A and the B lattice are equally affected. In contrast to a single

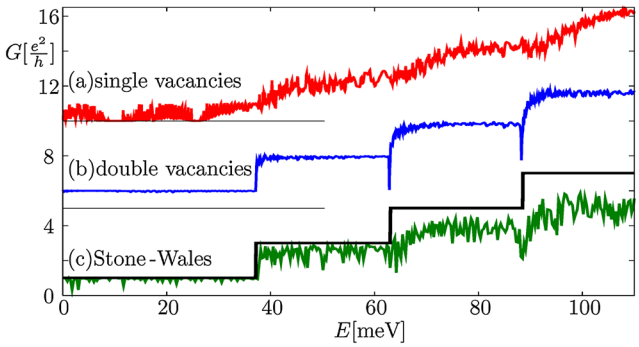

Figure 2 Quantum conductance G of a 60 nm wide graphene nanoribbon with a length of 1 μm and a defect density $n_i = 1 \times 10^{-5}$ defects/atom of (a) single-point vacancies, (b) double vacancies, or (c) Stone–Wales deformations (curves vertically offset by $5e^2/h$ for clarity). The staircase function for ideal size quantization plateaus is shown in (c) as thick black line.

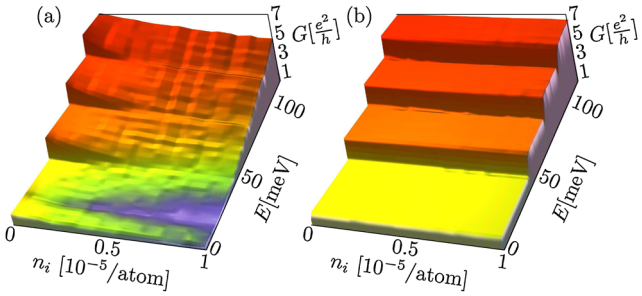

Figure 3 Quantum conductance G through a graphene zigzag nanoribbon of length 1 μm and width $W = 60$ nm as a function of energy and disorder concentration n_i (in units of 10^{-5} defects/atom) averaged over 100 disorder realizations for (a) single vacancies and (b) double vacancies.

vacancy, this defect therefore neither breaks the SU(2) pseudospin symmetry nor results in localized states [9]. A third and more complex defect of the ideal graphene lattice is the Stone–Wales deformation (SWd): four hexagons are replaced by two heptagon–pentagon pairs (see Fig. 1c). As a consequence, AB-scattering occurs. To first order approximation, we adapt the tight-binding parameters of the graphene ribbon to model the coupling parameters at the SWd using geometry-dependent coupling parameters.

4 Conductance in the presence of disorder We perform quantum transport simulations for a zigzag graphene nanoribbon of width $W = 60$ nm and length $L = 1$ μm in the presence of disorder. "Bulk" disorder is introduced by randomly distributed electronic lattice defects. Even relative defect concentrations as low as $n_i = 10^{-5}$ defects per atom give rise to pronounced deviations from the ideal staircase-shaped conductance G with plateaus due to transverse size quantization (see Fig. 2). Both single- and double vacancies lead to a reduction of transmission, yet the two types of vacancies give rise to very different modifications. While pseudospin conserving double vacancies approximately preserve the feature of quantization plateaus, with reduced height and pronounced dips near the steps where additional modes open, the quantization plateaus are completely washed out for single vacancies. This is all the more remarkable as the total number of point defects for single vacancies is only half the number for the double vacancies. The drastic difference between pseudospin conserving double vacancies and non-conserving single vacancies persists over a wide range of defect concentrations and is robust against an average over many disorder configurations (Fig. 3). Note that in experiment, the energy of the incoming electrons is usually modulated indirectly by a back gate voltage, which shifts the charge carrier density using capacitive coupling. While simple models predict a square root relation between back gate voltage and electron energy, a more quantitative treatment of the local device geometry is often needed [25, 26].

The connection between pseudospin conservation and transverse quantization steps can be inferred from the relation between the direction of the wave vector (Eq. (4)) and the helicity operator acting on the SU(2) representation-space spanned up by the A and B sublattices. For the free Dirac equation (Eq. (3)), the ratio between k_x and k_y is determined by the relative amplitude on the two sublattices, i.e., the pseudo-spin (see Eq. (5)). In turn, transverse quantization for a finite-width ribbon relates the step quantum number n with k_y. Consequently, the pseudospin degree of freedom is reflected in the size quantization in nanoribbons. Through the introduction of defects that break pseudospin conservation the transverse quantum number n becomes ill defined, resulting in the strong suppression of transverse quantization steps. The same is true for interactions with an underlying substrate, e.g., hexagonal boron nitride, which invariably introduces a spatially varying electronic potential $V(\mathbf{x})$ (see Eq. (3)). The absence of pronounced size-quantization plateaus in the experiment [28–32] points toward scattering at, e.g., rough edges [26] breaking pseudospin symmetry in experimental structures.

This mechanism can be illustrated and verified with the help of quasi-classical simulations based on the propagation of Monte-Carlo ensembles of classical trajectories: pseudospin conserving lattice defects are simulated by elastic scattering probabilities of the form of Eq. (6), pseudospin non-conserving defects will be represented by isotropic s-wave scattering (Eq. (7)). We randomly shoot trajectories that propagate classically (i.e., on straight lines) in between scattering events. After traversing on average a mean free path λ_s (determined by the disorder concentration), a scattering event with either pseudospin conserving or non-conserving angular differential scattering probability takes place. Note that the only quantum input are the differential scattering probabilities Eqs. (6) and (7). A trajectory is counted as transmitted (reflected) if it traverses the length $L \gg \lambda$ (or returns past the starting point).

As initial condition, we choose the longitudinal wave numbers $k_{x,n}$ corresponding to the quantized open modes n,

for each energy E

$$k_{x,n} = \sqrt{\left(\frac{E}{\hbar v_F}\right)^2 - \left(\frac{n\pi}{W}\right)^2}, \quad n \in \mathbb{Z}. \tag{8}$$

We use, typically, 200.000 trajectories per scattering channel with initial momenta chosen according to Eq. (8). If the mismatch $|k_y - k_{y,n}|$ between the transverse wave number k_y and $k_{y,n}$ corresponding to the largest flux-carrying mode (i.e., the largest n for which $k_{x,n}$ is real) is larger than $|k_y - k_{y,n+1}|$, scattering into an evanescent mode (i.e., complex k_x) is assumed, initiating a new scattering event in backward direction $(-k_x, k_y)$. The average over ensembles of trajectories provides a quasi-classical Monte-Carlo estimate for the conductance as a function of energy.

Using either an angular dependent scattering probability for scattering at point defects that are pseudospin preserving (Eq. (6)) or non-conserving (Eq. (7)), we can reproduce all qualitative features of the full quantum conductance simulations in remarkable detail (Fig. 4): for s-wave scattering, quantization steps are strongly suppressed, yielding an (approximately) linear slope of transmission with energy. For pseudospin-conserving scattering, quantization steps survive, and the characteristic dips in the transmission near the thresholds observed in the full quantum mechanical calculation are reproduced. These dips resulting from scattering into evanescent modes disappear in the case of s-wave scattering because the isotropically scattered portion of the wave retains no information on the direction prior to the scattering event. Our quasi-classical model thus provides simple qualitative explanations for the full quantum-mechanical calculations, even though it does not include self-focusing due to the wave nature of the charge carriers is not included or diffractive scattering. We have verified (not shown) that the striking differences between single- and double vacancy scattering are not qualitatively changed by higher-order effects (e.g. trigonal warping). The relation between broken SU(2) pseudospin symmetry and the destruction of size-quantization plateaus implies that for disorder caused by different and more complex defects which also result in pseudospin non-conserving scattering, signatures of transverse quantization should also disappear [26]. This can, indeed, be verified for Stone–Wales defects [Fig. 1(c)]. The size quantization plateaus are washed out also here by as few as 1 SWd in 10^5 atoms (see Fig. 2c).

5 Weak localization We now turn our attention to transport in the presence of a weak perpendicular magnetic field. In conventional semiconductors, coherent backscattering leads to weak localization, an enhancement of resistance for zero magnetic fields [33]. From a semiclassical point of view, each trajectory contributing to reflection has a time-reversed partner, that is transversed in the opposite direction. Since both trajectories will accumulate the same phase, they interfere constructively. At finite magnetic fields B, however, the additional Aharonov–Bohm phase features opposite signs for the two paired trajectories, destroying the

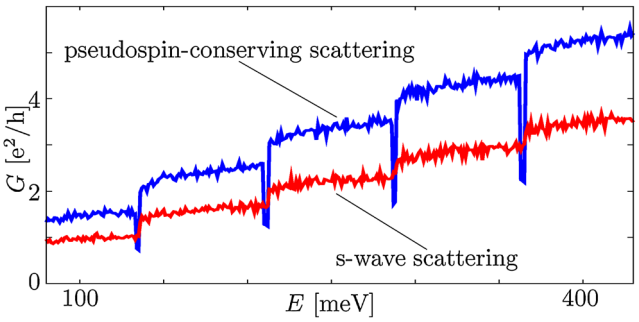

Figure 4 Quasi-classical Monte-Carlo simulation of transport through a disordered nanowire, using a Dirac-like linear dispersion relation, and either pseudospin-conserving scattering (upper blue line) or s-wave scattering (lower red line) at randomly distributed local defects.

constructive interference between time-reversed reflection pathways. When plotting the reflection or, equivalently, the resistance as a function of magnetic field, one thus finds a peak at zero field strength and, through unitarity, a corresponding dip in transmission. The characteristic width of this peak is related to the average accumulated phase difference $\langle\Delta\phi\rangle$ between a trajectory and its time-reversed partner. $\Delta\phi$ is proportional to the enclosed magnetic flux Φ, $\langle\Delta\phi\rangle = 2\pi\Phi/\Phi_0 = 2\pi B \cdot \langle A\rangle / \Phi_0$, where $\langle A\rangle$ is the average area enclosed by trajectories and Φ_0 is the magnetic flux quantum. For random scattering among the defects we estimate that after a time τ the enclosed area $\langle A\rangle \approx \lambda_e v_F \tau$, where λ_e is the elastic mean free path. As $\langle\Delta\phi\rangle$ reaches 2π, a given trajectory no longer contributes to weak localization.

$$\langle\Delta\phi\rangle = \frac{2\pi B \cdot \langle A\rangle}{\Phi_0} = 2\pi \rightarrow \tau_B = \frac{\Phi_0}{\lambda_e v_F B}, \tag{9}$$

where τ_B represents the time scale after which the phase accumulated by the magnetic field B is of the order of 2π.

For transport through bulk-disordered graphene the situation is more involved [34]. Since pseudospin conservation leads to a suppression of backscattering (see Eq. (6)), one would expect a suppression of reflection at zero magnetic field. Indeed, each individual Dirac cone is not time-reversal invariant by itself (due to the additional Berry phase of π associated with pseudospin), resulting in destructive interference for a trajectory and its time-reversed path. Thus, ideal graphene features a weak antilocalization dip in resistance R or a weak antilocalization peak in conductance G. (In order to avoid confusion we will refer in the following only to the properties of G). Likewise, conventional localization manifests itself as a dip in G. The antilocalization peak in G hinges on the absence of both inter-valley scattering (characterized by a time-scale τ_i) and of intra-valley scattering (characterized by τ_z). Inter-valley scattering invalidates the single-Dirac-cone picture thus leading to conventional localization (dip in G) while intra-valley scattering randomizes pseudospin and suppresses any weak (anti)localization effect [34]. In light of our previous results, we therefore expect a weak

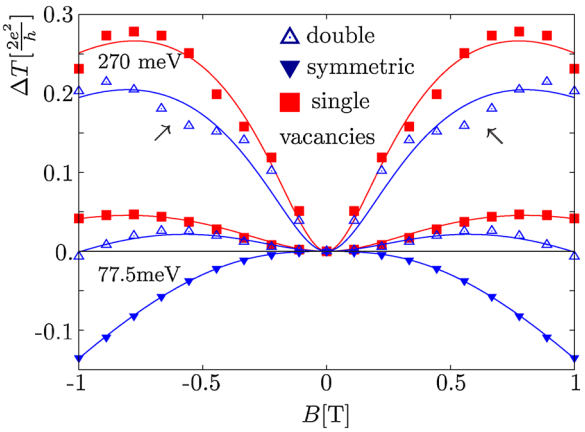

Figure 5 Conductance (ΔT) as function of perpendicular magnetic field B for 60 nm wide ribbons with single (red squares) and double (blue triangles) vacancies, at two energies (see the label). Curves are fits to Eq. (10), for fit parameters see Table 1. Black arrows mark an oscillation not reproduced by Eq. (10).

localization dip in the presence of single vacancies ($\tau_z \gg \tau_i$), and no localization effect, or even a weak anti-localization peak, in the presence of double vacancies ($\tau_i \gg \tau_z$).

A requirement for a weak antilocalization peak is destructive interference of a reflected trajectory and its time-reversed partner. The Berry phase associated with the conical bandstructure of graphene leads to this exact cancelation if we assume a perfect cone structure. However, if the accumulated phase difference is randomized, either by intravalley scattering (small τ_z) or by dephasing by trigonal warping (small τ_W) for energies further away from the Dirac point, the accumulated relative phase will differ from the mean value of π for the Berry phase and suppresses antilocalization. By contrast, the conventional weak localization dip in G due to inter-valley scattering (τ_i) is not affected by trigonal warping, as K and K' are deformed in an identical way.

We investigate the magnetic-field dependence of the conductance in the presence of single and double vacancies, taken as prototypical cases of pseudo-spin conserving and pseudo-spin breaking scattering. Note that proper treatment of the intermediate case of a Stone–Wales defect in a magnetic field would require a full density functional theory parametrization, which is beyond the scope of this work. At moderate energies ($E = 77.5$ meV), we find a weak antilocalization peak in G for the case of double vacancy defects (Fig. 5). With increasing distance in energy from the Dirac point ($E = 280$ meV), the conventional localization dip becomes more pronounced as the dephasing due to trigonal warping (smaller τ_W) becomes significant resulting in a narrow localization dip on top of an underlying broad antilocalization maximum (Fig. 5). Long trajectories feature multiple scattering events, incorporate a substantial amount of inter-valley scattering, and thus contribute to the localization dip. By contrast, short trajectories may still contribute to the antilocalization peak, as they enclose smaller areas. Consequently, the residue of the antilocalization peak extends to higher field strengths.

Even for only a few double vacancies at low energies, the antilocalization peak is substantially reduced. This might be related to the additional internal degree of freedom for disorder of double vacancies: the angle of orientation α of the lattice vector connecting the two vacancies relative to the ribbon axis. Previously, we assumed a random orientation with equal statistical weight for all three possible orientations of double vacancies (DV, see open blue triangles in Fig. 5). To obtain more pronounced antilocalization features, we consider symmetric double vacancies (SDV, see full blue triangles in Fig. 5), where we fix the alignment of the axis through the two missing carbon atoms orthogonal to the direction of transport. Indeed, the localization dip vanishes, and we only find pronounced antilocalization for this system, showing the pronounced sensitivity of transport in graphene to local symmetries (see full triangles in Fig. 5).

To make the present analysis more quantitative, we fit our data by the weak (anti-) localization approximation for diffusive transport in disordered graphene [34, 35]

$$\Delta T = \frac{e^2}{h}\left[F\left(\frac{\tau_B^{-1}}{\tau_D^{-1}}\right) - F\left(\frac{\tau_B^{-1}}{\tau_D^{-1}+2\tau_i^{-1}}\right) - 2F\left(\frac{\tau_B^{-1}}{\tau_D^{-1}+\tau_*^{-1}}\right)\right], \tag{10}$$

$$F(x) = \log(x) + \digamma\left(\frac{1}{2}+\frac{1}{x}\right), \tag{11}$$

$$\tau_*^{-1} = \tau_i^{-1} + \tau_W^{-1} + \tau_z^{-1}, \tag{12}$$

where $\digamma$ denotes the digamma function, and τ_D the dwell time in the cavity and τ_*^{-1} is the total scattering and dephasing rate. Note that the above formulas where originally derived for diffusive transport, where the major contribution to weak localizations comes from paths of virtually excited electron-hole pairs [36]. Suppression of weak localization in the experiment points toward decrease of the relevant time scales by disorder or strain effects [19]. In ballistic transport, the Aharonov–Bohm phase replaces this contribution, while the origin of the different contributions to (anti-)localization should be, to first order, the same. Our nanoribbons feature a low disorder concentration and are not perfectly ballistic. Even though the underlying processes contributing to either localization or anti-localization are different in the ballistic and diffusive regimes, the net effect on the (anti-) localization curve is the same. We thus use the parametrized lineshapes of Eq. (10) to compare the relative prefactors associated with scattering events leading to either weak localization or weak antilocalization.

Extracting three different time scales from the shape of a single weak localization curve may lead to ambiguous fits. We therefore exploit the fact that the dwell time τ_D only depends on the electron energy (and not the disorder, [37]): different defect types at the same energy should result in the

Table 1 Scattering times used to fit the calculated transmission data (see Fig. 5) for single vacancies (SV), double vacancies (DV), and symmetric double vacancies (SDV) at different energies. Values set in bold text where fitted using Eq. (10), while values set in normal text where taken from the corresponding fitted configuration (see text).

defect	energy [meV]	τ_D/τ_B	τ_i/τ_B	τ_*/τ_B
SDV	75	**3.9**	**7.1**	**7.0**
DV	75	3.9	**6.5**	**3.3**
DV	280	**8.5**	6.5	**3.7**
SV	75	3.9	**5.9**	**2.6**
SV	280	8.5	5.9	**2.9**

same τ_D. Likewise, the inter-valley scattering time τ_i should only depend on the defect type (i.e., single, double, and symmetric double vacancies). We thus fit the dwell time τ_D for the case of SDVs at each energy (bold-face entries in Table 1), and use identical values of τ_D for DV and SV defects (normal-face entries in Table 1). Likewise, we only fit one τ_i for each defect type (SDV, DV, SV), and use this value for both energies. We find that with these constraints we can fit the numerical data very well, especially for symmetric double vacancies (see solid lines in Fig. 5). There is, however, an oscillation superimposed on the magnetoconductance unaccounted for by Eq. (10) (see black arrows in Fig. 5) that we relate to the shift of the conductance step by the magnetic field. Since conductance steps are much less pronounced for single vacancies, we do not observe a similar feature in the single vacancy data (see red squares in Fig. 5). Comparing the specific scattering rates, we find a strong decrease in τ_* when comparing nanoribbons with single to those with double vacancies (about 20%, see Table 1). τ_* is dominated by the smallest scattering time of τ_i, τ_W and τ_z (see Eq. (12)). Since the relative change in τ_i is small (see Table 1), and the trigonal warping scattering time τ_W only depends on energy, a substantially reduced intra-valley scattering time τ_z is responsible for the reduction in τ_*. Our analysis of weak localization, thus, quantitatively confirms that single vacancies lead to substantial intra-valley scattering which breaks pseudospin and, in turn, washes out signatures of size quantization.

6 Conclusions We have presented full quantum transport simulations through disordered graphene nanoribbons of realistic size and find that even very low concentrations of single defects destroy the graphene pseudospin symmetry leading to a destruction of transverse size quantization plateaus in the conductance. By contrast, randomly distributed double defects that equally affect both sublattices and, thus, preserve the SU(2) pseudospin symmetry, leave the quantization plateaus intact while modifying the transmission function. Our present results suggest that the difficulty in observing pronounced quantization plateaus in the conductance may be related to the presence of pseudospin non-conserving defects. Indeed, in agreement with these results, recent studies demonstrate that plateaus of quantized conductance can be observed if graphene quantum point contacts are both suspended from the substrate and thoroughly annealed to reduce the number of adsorbates on the graphene lattice. We show that the investigation of weak localization at low energies can be a powerful tool to determine symmetry properties of graphene nanoribbons. Weak antilocalization indicates high symmetry and approximate pseudospin conservation. A fit to a theoretical model [34] allows us to extract the relative strength of inter-valley and intra-valley scattering. Combining the information on measured size quantization plateaus and weak (anti)localization peaks allows us to probe the dynamics of short and long scattering paths. Such measurements could thus be used as a tool to characterize the scattering behavior of different probes, and ultimately to identify and improve fabrication of pseudospin conserving samples.

Acknowledgements We thank C. Lewenkopf and C. Stampfer for valuable discussions. Support by the Austrian Science Fund, ViCoM SFB-041-P05 and NextLite SFB049-P04 is gratefully acknowledged. S. R. acknowledges support by the Austrian Science Fund (FWF) through projects SFB-F49-P10 NextLight and GePartWave (I1142). Numerical calculations were performed on the Vienna scientific cluster (VSC2).

References

[1] K. S. Novoselov, A. K. Geim, S. V. Morozov, D. Jiang, M. I. Katsnelson, I. V. Grigorieva, S. V. Dubonos, and A. A. Firsov, Nature **438**, 197 (2005).
[2] A. H. C. Neto, F. Guinea, N. M. R. Peres, K. S. Novoselov, and A. K. Geim, Rev. Mod. Phys. **81**, 109 (2009).
[3] M. Wimmer, A. R. Akhmerov, and F. Guinea, Phys. Rev. B **82**, 045409 (2010).
[4] E. R. Mucciolo, A. H. CastroNeto, and C. H. Lewenkopf, Phys. Rev. B **79**, 075407 (2009).
[5] A. Cresti, F. Ortmann, T. Louvet, D. V. Tuan, and S. Roche, Phys. Rev. Lett. **110**, 196601 (2013)
[6] S. Ihnatsenka and G. Kirczenow, Phys. Rev. B **85**, 121407 (2012).
[7] S. Yuan, H. De Raedt, and M. I. Katsnelsion, Phys. Rev. B **82**, 115448 (2010).
[8] A. Cresti, and S. Roche, Phys. Rev. B **79**, 233404 (2009).
[9] V. M. Pereira, J. M. B. Lopes dos Santos, and A. H. Castro Neto, Phys. Rev. B **77**, 115109 (2008).
[10] J. Wurm, M. Wimmer, and K. Richter, Phys. Rev. B **85**, 245418 (2012).
[11] M. Evaldsson, I. V. Zozoulenko, H. Xu, and T. Heinzel, Phys. Rev. B **78**, 161407(R) (2008).
[12] F. Libisch, S. Rotter, and J. Burgdörfer, New J. Phys. **14**, 123006 (2012).
[13] H.-Y. Deng and K. Wakabayashi, Phys. Rev. B **90**, 115413 (2014)
[14] H.-Y. Deng and K. Wakabayashi, Phys. Rev. B **91**, 035425 (2015)
[15] A. R. Botello-Méndez, A. Lherbier, and J.-C. Charlier, Solid State Commun. **175**, 90 (2013).
[16] A. Lherbier, B. Biel, Y.-M. Niquet, and S. Roche, Phys. Rev. Lett. **100**, 036803 (2008).
[17] P. Scuracchio, S. Costamagna, F. M. Peeters, and A. Dobry, Phys. Rev. B **90**, 035429 (2014).

[18] P. R. Wallace, Phys. Rev. **71**, 622 (1947).
[19] S. V. Morozov, K. S. Novoselov, M. I. Katsnelson, F. Schedin, L. A. Ponomarenko, D. Jiang, and A. K. Geim, Phys. Rev. Lett. **97**, 016801 (2006)
[20] S. Rotter, J. Z. Tang, L. Wirtz, J. Trost, and J. Burgdörfer, Phys. Rev. B **62**, 1950 (2000).
[21] G. W. Semenoff, Phys. Rev. Lett. **53**, 2449 (1984).
[22] G. T. de Laissardière, Phys. Rev. Lett. **111**, 146601 (2013)
[23] F. Ducastelle, Phys. Rev. B **88**, 075413 (2013)
[24] M. M. Ugeda, I. Brihuega, F. Hiebel, P. Mallet, J.-Y. Veuillen, J. M. Gómez-Rodríguez, and F. Ynduráin, Phys. Rev. B **85**, 121402(R) (2012).
[25] R. Reiter, U. Derra, S. Birner, B. Terrès, F. Libisch, J. Burgdörfer, and C. Stampfer, Phys. Rev. B **89**, 115406 (2014).
[26] B. Terrès, L. A. Chizhova, F. Libisch, J. Peiro, D. Jörger, S. Engels, A. Girschik, K. Watanabe, T. Taniguchi, S. V. Rotkin, J. Burgdörfer, and C. Stampfer, Nature Commun. **7**, 11528 (2016).
[27] F. Libisch, S. Rotter, and J. Burgdörfer, Phys. Status Solidi B **248**, 2598 (2011).
[28] M. Y. Han, J. C. Brant, and P. Kim, Phys. Rev. Lett. **104**, 056801 (2010).
[29] F. Molitor, A. Jacobsen, C. Stampfer, J. Güttinger, T. Ihn, and K. Ensslin, Phys. Rev. B **79**, 075426 (2009).
[30] Y.-M. Lin, V. Perebeinos, Z. Chen, and P. Avouris, Phys. Rev. B **78**, 161409 (2008).
[31] E. R. Mucciolo and C. H. Lewenkopf, J. Phys.: Condens. Matter **22**, 273201 (2010).
[32] N. Tombros, A. Veligura, J. Junesch, M. H. D. Guimarães, I. J. Vera-Marun, H. T. Jonkman, and B. J. van Wees, Nature Phys. **7**, 697 (2011).
[33] D. K. Ferry and S. M. Goodwick, Transport in Nanostructures (Cambridge University Press, Cambridge, 1999).
[34] E. McCann, K. Kechedzhi, V. I. Fal'ko, H. Suzuura, T. Ando, and B. L. Altshuler, Phys. Rev. Lett. **97**, 146805 (2006).
[35] F. V. Tikhonenko, D. W. Horsell, R. V. Gorbachev, and A. K. Savchenko, Phys. Rev. Lett. **100**, 056802 (2008).
[36] B. L. Altshuler, D. Khemlnitski, A. I. Larkin, and P. A. Lee, Phys. Rev. B **22**, 5142 (1980).
[37] R. Pierrat, P. Ambichl, S. Gigan, A. Haber, R. Carminati, and S. Rotter, Proc. Natl. Acad. Sci. USA **111**, 17765 (2014).